Spur-Free Dynamic Range Measurements of a Differentially Driven Traveling Wave Mach-Zehnder Carrier Depletion Silicon Modulator

Matthew Streshinsky

A thesis

submitted in partial fulfillment of the

requirements for the degree of

Master Of Science In Electrical Engineering

University of Washington

2012

Committee

Michael Hochberg

Mani Soma

Program Authorized to Offer Degree:

Electrical Engineering

University of Washington

Abstract

Spur-Free Dynamic Range Measurements of a Differentially Driven Traveling Wave Mach-Zehnder Carrier Depletion Silicon Modulator

Matthew Streshinsky

Chair of the Supervisory Committee:
Michael Hochberg
Assistant Professor of Electrical Engineering

An outstanding question has been whether the analog performance of silicon components can compete with conventional optical material systems such as Lithium Niobate. A key challenge for silicon photonics is the fact that most modulators, including the one reported here, are based on a reverse biased PN junction. PN junctions exhibit significant nonlinearities, and it has thus been unclear whether analog performance in the silicon platform could ever compete with what has been achieved with Lithium Niobate based modulators.

Characterized here is one of the key metrics for analog performance, the Spur Free Dynamic Range (SFDR). This is a measure of the degree of nonlinear cross-talk between different frequencies propagating in a single system. With the proper device configuration, this work shows that the SFDR of a silicon modulator can approach that of Lithium Niobate based systems. In particular, this modulator achieves 104.5 $\mathrm{dB{\cdot}Hz}^{2/3}$ SFDR for IMD, which is within 15 dB of the best result in Lithium Niobate, 120.5

dB·Hz$^{2/3}$. This level of performance is also already sufficient for a number of analog applications, including WLAN. The paths to improving this value are also briefly discussed; there are a number of reasons to believe that performance in integrated silicon photonic systems can be improved in the future, and likely match the performance seen in the very best optical systems for analog links.

Table of Contents

List of Figures

Chapter 1 Silicon Photonics

1.1 Introduction

In 1969, Stewart Miller described a future in which optical circuits could be integrated onto a single chip [1]. While his work references materials such as Lithium Niobate and III-V semiconductors, the emergence of silicon as the dominant semiconductor platform led to further research into the optical capabilities of the silicon platform. Richard Soref and Brian Bennett's 1987 paper [2], in which they describe the carrier-induced change in index of refraction, led to profound innovations in the field of integrated optics. While their paper focuses on the change in index of refraction in silicon at different carrier concentrations, the paper has extremely diverse applications in telecommunications, biological sensing, military radar, optical sensors, signal processing, and biological labs-on-chip. By demonstrating the possibility of active optical devices fabricated in silicon, they had demonstrated the potential for complex integrated optical systems to be fabricated next to conventional electronic circuitry.

Silicon is an attractive medium to fabricate high-speed optical devices primarily due to the ability to integrate very complex optical systems for potentially low costs. Significant investments have already been made in semiconductor manufacturing, and silicon photonics possesses the capability to share foundry resources and leverage manufacturing techniques with these conventional CMOS electronics processes [5],[6].

Additionally, silicon provides unique form factors in each of these applications by allowing for the integration of many devices onto a single silicon wafer. There may be applications in which a stand-alone modulator-fiber-detector scheme is too bulky or otherwise unattractive and in which silicon could compact the design onto a single chip.

While these applications are exciting, one may argue that silicon is not the ideal material system in which to develop devices—other materials such as Lithium Niobate and group III-V semiconductors have demonstrated better performance in most metrics. However, silicon photonics does have the distinct advantage of being able to be co-located with conventional microelectronics and leverage existing fabrication technologies to produce high-yield devices and systems. With these factors, silicon photonics becomes attractive for some combination of high-volume, shared production, or high yield-requiring applications [3].

1.2 Silicon Modulators

Optical devices fabricated in the silicon material system have shown promise for use in high-speed integrated analog optical links [7]. In particular, traveling wave Mach-Zehnder silicon modulators have been shown as promising candidates for high speed and low drive voltage transmission [8]-[10] in optical links.

One important performance metric for an analog optical link is spur-free dynamic range (SFDR) [11]-[15]. A silicon modulator with a high SFDR allows for its use in analog applications such as SATCOM [16] or RF-over-fiber communication systems [11],[17]. For example, for WLAN systems, an SFDR of $95\,\mathrm{dB\cdot Hz^{2/3}}$ is typically required [17]. However, due to the nature of carrier-depletion modulation, the transfer function contains additional nonlinearities not exhibited in a linear electrooptic modulation scheme.

This work characterizes the nonlinearity of a traveling wave Mach-Zehnder carrier depletion silicon modulator fabricated through the Insitute of Microelectronics at A*STAR in Singapore. I show that the linearity of a silicon travelling wave Mach-

Zehnder modulator can be improved by differentially driving it. Spurious free dynamic range for intermodulation distortion of as high as 104.5 dB·Hz$^{2/3}$ is obtained. This is in close agreement with theoretical predictions in which the pn junction nonlinearity is the primary source of distortion.

1.3 Previous Work

There has already been a considerable amount of work characterizing the linearity of Mach-Zehnder modulators in other material systems. Williams *et al*. used a high-power photodetector to measure the nonlinearity of a Lithium Niobate modulator of 119.5 dB·Hz$^{2/3}$ [21]. By biasing the modulator past quadrature to improve the noise figure Karim and Devenport demonstrated an SFDR of 120.5 dB·Hz$^{2/3}$ [20]. Additionally, Electroabsorption modulators have a bias point that minimizes third order distortion and have demonstrated some of the relatively largest SFDRs for a simpe modulator design. The authors of [22] demonstrated an SFDR of 128 dB·Hz$^{4/5}$ in an electroabsorption modulator at 10 GHz.

Recently, Ayazi *et al.* have characterized the nonlinearities in a silicon ring modulator and found a third-order limited SFDR as high as 84 dB·Hz$^{2/3}$ [18]. Their results presented the first measurement of the nonlinearity of a silicon modulator. Additionally, Lo *et al.* have made theoretical predictions for the SFDR of a p-i-p-i-n diode-based silicon MZM of 115.4 dB·Hz$^{2/3}$ [19]. Their work found that the nonlinearity of the p-i-p-i-n junction counteracted the transfer function nonlinearity inherent in a Mach-Zehnder interferometer.

Chapter 2 Mach-Zehnder Modulators

2.1 Fundamental Building Blocks

This section will briefly introduce the principal components that are required in the design and test of a silicon Mach-Zehnder modulator. A sketch of the general geometry of one arm of the Mach-Zehnder interferometer is shown below.

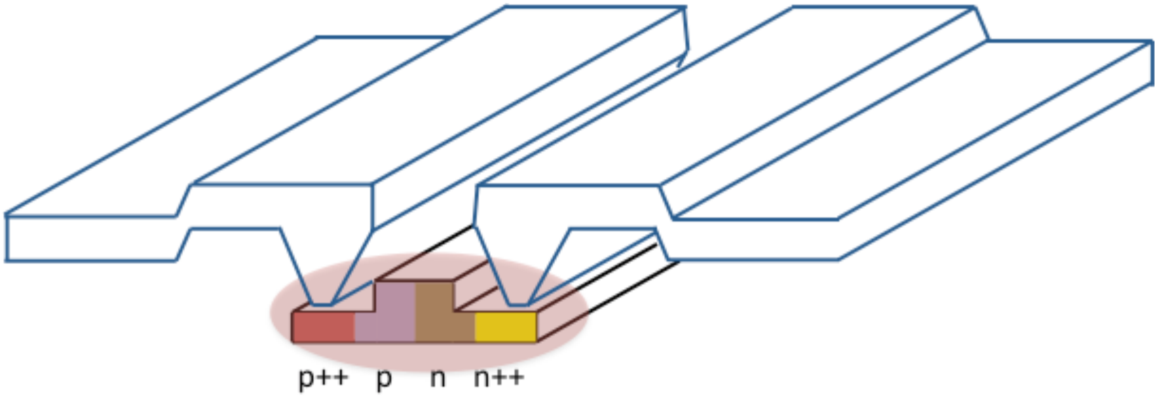

Figure 1. Cross-section diagram of one arm of a Mach Zehnder modulator

Waveguides

A rib waveguide, pictured above, doped with a p++, p, n, and n++ dopants is used in this modulator. A wide silicon rib region is used in order to minimize the abosrption by the metal contacts and transmission lines. If the channel region is 220 nm thick and 500 µm wide, a single optical mode propagates at 1550 nm. Details of the fabrication are discussed later in this chapter.

Grating Couplers

Holographic lenses are used in order to couple light onto and off of the silicon wafer from and to an optical fiber. Such a device consists of a periodic structure that refracts the vertical incident light into a waveguide in the surface plane of the wafer. The grating couplers used for this test typically provided -4.3 dB coupling efficiency.

Y-Junction

A y-junction is used in order to split and recombine the two optical paths of a Mach-Zehnder interferometer. 1.3 dB of excess loss was typical for this test.

Phase Shifters

By doping a silicon waveguide, the index of the silicon may be modified via the plasma dispersion effect (discussed further in the following section). Changing the bias voltage of a pn junction can then be used to control the optical path length of a length of doped silicon waveguides.

2.2 Modulation Mechanism

Modulation in a Mach-Zehnder modulator is achieved by varying the relative phase of each arm of the modulator. For a differentially driven modulator, opposite phase shifts are applied to each arm. In the case of the silicon carrier depletion Mach-Zehnder presented here, the voltage across a waveguide doped with a pn junction is modulated in order to induce a phase shift in each arm due to carrier refraction.

As mentioned in Chapter 1, Soref and Bennett first characterized the change in index in silicon due to carrier refraction by analyzing previously published results of the absorption spectra of crystalline silicon at various doping densities. For comparison to an electric-field induced change in index, they also examined the absorption spectra at various electric field strengths. From these previous results, they derived expected index changes two orders of magnitude greater for carrier-induced index change than that of electric field-induced index change. Schmid published data on the absorption of n-type and p-type silicon at doping concentrations in the 10^{18} to 10^{20} cm^{-3} ranges in 1981. Additionally, in 1957 Spitzer and Fan published on the absorption of n-type silicon in the infrared range. These previous results were used as the basis for a Kramers-Kronig analysis to predict the change in refractive index of silicon.

The relationship between index of refraction and absorption can be written as the Kramers-Kronig relation:

$$n(\omega) = \frac{c}{\pi} \mathrm{P} \int_0^{\infty} \frac{\Delta\alpha(\omega')d\omega'}{\omega'^2 - \omega^2} \tag{1}$$

Thus, given data on the absorption spectra, one could numerically integrate according to (1) to determine an approximate value for refractive index. Although for each wavelength of interest the integral extends to infinity over the entire range of absorption, for wavelengths $\omega' \gg \omega$, the integral quickly approaches zero. Thus, as long as absorption data extends significantly beyond the wavelength range of interest, this is not an issue and the numerical method will be a sufficiently close approximation.

Since silicon does not allow for the Pockels effect due to the centrosymmetry in its crystal lattice, conventional methods of electrooptical modulation, used in Lithium Niobate and other material systems, are not viable in silicon [4]. The change in refractive index due to an electric field in silicon is primarily due to the Franz-Keldysh effect wherein an electric field causes the wavefunctions of electrons and holes to overlap and increase the rate of optical absorption. The Kerr effect is also present in which the change in index is proportional to the square of applied field [2].

Soref and Bennett calculate a change in index for the Franz-Keldysh effect of $\Delta n = 10^{-4}$ at a field of $E = 2 \times 10^5 \frac{V}{cm}$ and a wavelength of 1.07 μm. They also calculate the index change due to the Kerr effect of $\Delta n = 10^{-4}$ at an electric field of $E = 10^6 \frac{V}{cm}$ and a wavelength of 1.3 μm. With such a conditions, a one-micron wide waveguide 1 millimeter in length would require more than 100 Volts across the waveguide to achieve a 180° phase shift. These parameters are typically unacceptable for fabrication of a viable electrooptic device.

Carrier refraction, on the other hand, is shown to have a much stronger effect in silicon than electric field refraction. Three principle effects contribute to carrier refraction: free carrier absorption, Burnstein-Moss bandfilling, and Coulombic interaction of carriers with impurities. Free carrier absorption is an intraband transition of an electron or hole and is proportional to the square of wavelength and approximately linear with carrier concentration [23]. In Burnstein-Moss bandfilling, the energy gap between the top of the valence band and the unoccupied states in the conduction band shifts with doping level. This shift is caused by the Fermi energy moving into the conduction band (n-type) or valence band (p-type) and blocking optical excitations [24]. In the third carrier refraction effect, Coulombic interactions, ionized impurities create a Coulombic force that can deflect an electron or hole, thereby reducing the mobility of these free carriers [25].

Soref and Bennett analyzed doping concentrations in the range of 10^{17} to 10^{20} cm^{-3}, which are readily achievable in common semiconductor manufacturing. From a Kramers-Kronig analysis, the following relation for index change at a wavelength of 1550 nm is found:

$$\Delta n = \Delta n_e + \Delta n_h = -[8.8 \times 10^{-22}\, \Delta N_e + 8.5 \times 10^{-18} (\Delta N_h)^{0.8}] \qquad (2)$$

where N_e and N_h are the electron and hole densities in units of cm^{-3}. The authors also note that the depletion operation mode has a response on the order of picoseconds, and predict that the bandwidth of such a device is likely limited by the electrical RC time constant.

Using finite element simulation software, the effective index, n_{eff}, may be solved at different concentrations of charge carriers in the waveguide. To do this, a device modeling software package such as Sentaurus could be used to analyze the electron and hole distribution under different bias conditions. From this distribution, the following overlap integral over the carrier depletion region may be performed:

$$\Delta n_{eff} = \frac{\iint_S \Delta n(x,y)|E(x,y)|^2 dxdy}{\iint_S |E(x,y)|^2 dxdy} \tag{3}$$

where E is the electric field distribution of the optical mode obtained from the finite element solution of the waveguide. Given Δn_{eff} at various wavelengths, the total phase shift of one arm of the modulator can be determined by:

$$\Delta\phi = \frac{2\pi}{\lambda} \Delta n_{eff} L \tag{4}$$

where L is the total length of the phase shifter. This analysis may be done at a variety of bias voltages in order to predict the n_{eff} and phase vs. bias voltage characteristics of the device. The importance of the linearity of knowing this relationship will be discussed further in the next section.

The arms of a Mach-Zender interferometer may be doped such that varying the bias across the pn junction may control the relative phase of each arm. In this configuration, a Mach-Zehnder will have transfer function:

$$I_{out} = \frac{G I_{in}}{2} [\cos(\phi)] \tag{5}$$

where I_{in} is the intensity of light input to the device, G is the device insertion loss, and ϕ is the relative phase shift between each arm of the modulator.

2.3 Reverse Biased PN Junctions

In order to modulate the carrier concentration in the waveguide section of the Mach-Zehnder modulator, a reverse biased pn junction is used. The width of the depletion region is modulated by an applied electric signal across the junction. As mentioned in the previous section, the resulting change in carrier concentration induces a change in the index of the material and, consequently, a change in the effective index of the propagating mode. This type of junction is often used due to the compatibility with CMOS processes and very high bandwidths attainable in such a design. Currently the highest bandwidth device using a pn junction is 30 GHz [26].

Knowing the relationship between n_{eff} and reverse bias in the pn junction is critical to device design. One can obtain this relationship using the simulation tool Sentaurus-process to generate doping concentrations in the waveguide at different reverse bias conditions and Equation (3). This data has been previously presented in [18], and is plotted below:

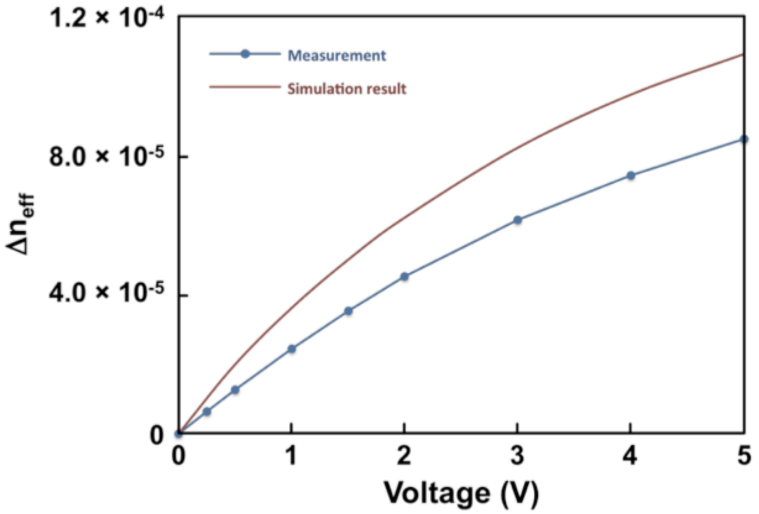

Figure 2. n_{eff} vs reverse bias voltage in the pn junction used in the modulator studied in this work. Plot from [18]

Importantly, the capacitance of the junction also changes with voltage. For modulator bandwidths that are limited by the RC time constant of the junction, a lower junction capacitance is desired. Additionally, as will be discussed in the next section, the junction capacitance is an important consideration in the rf design. Data for the modulator studied in this work is previously presented in [27] and is also plotted for reference below:

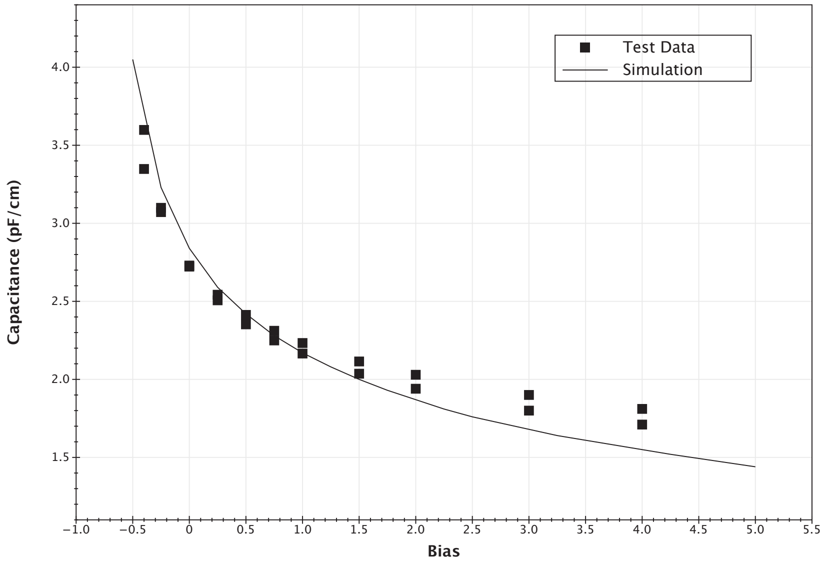

Figure 3. Capacitance vs. reverse bias voltage across the pn junction used in the modulator. Plot and data from [27].

2.4 Traveling Wave Design

In order to improve the performance of a Mach-Zehnder modulator, a traveling wave design is often used. In this geometry, the modulator is designed such that the electrical mode propagates at the same rate as the optical mode. Since the doping concentrations are often not in the designer's control, the RF engineering becomes one of the more important components of this type of modulator design.

For traveling wave devices, two fundamental limits on device bandwidth are the RC time constant of the pn-junction in the waveguide and the RF loss of the transmission line. There are additional limitations in the reflections from RF connections, but these tend to be less significant. The traveling wave design enables the designer to lower the required voltage swing for a π phase shift by extending the length of the device. The additional length, however, decreases the device bandwidth due to RF losses as well as introduces additional optical insertion loss.

The transmission line may be represented by the circuit:

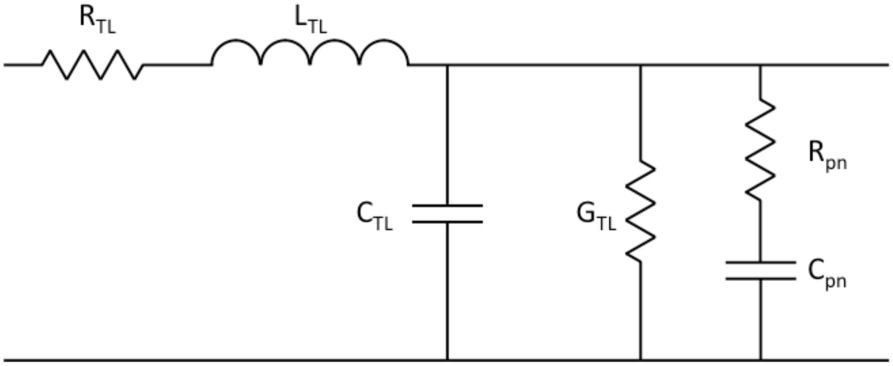

Figure 4. Transmission line equivalent circuit element

where R_{TL}, is the parasitic resistance of the transmission line, L_{TL} is the self-inductance, C_{TL} is the capacitance between the conductor and the substrate, G_{TL} is the resistance between the conductor and subsrate, and R_{pn} and C_{pn} are the resistance and capacitance from the junction. In reality, G_{TL} is usually negligible.

In the low loss limit ($R_{TL} \rightarrow 0, G_{TL} \rightarrow \infty$), the following equations hold:

$$\gamma \approx -\sqrt{L_{TL}\left(C_{pn} + C_{TL}\right)}\omega \tag{6}$$

$$Z \approx \sqrt{\frac{L_{TL}}{C_{pn} + C_{TL}}} \tag{7}$$

$$n_{RF} = \frac{\gamma c}{\omega} \tag{8}$$

Since the basic premise of a traveling wave modulator is to let the electrical mode flow with the optical mode, it is important to match n_{RF} to the optical index. In the case of silicon modulators, ideally it would be favorable such that errors in the mismatch of modes favor the optical mode. Optical delay lines are relatively trivial to fabricate when compared to the design effort needed for RF electrical delay lines.

2.5 Figures of Merit

There are several figures of merit with which to characterize the performance of a Mach-Zehnder Modulator. Presented here are V_π, $V_\pi L$, bandwidth, insertion loss, and SFDR. Noise figure, which is not measured in this work, describes the signal to noise degradation from signal input to output. The first figure of merit, V_π, is the voltage required to achieve a π phase shift. A common value reported in addition to this metric is $V_\pi L$, which is simply V_π multiplied by the length of the phase shifter. In this way, $V_\pi L$ normalizes V_π for different modulator lengths. Insertion loss is the optical loss introduced by the modulator. This loss comes from a variety of sources including: loss due to the waveguide and dopant materials, coupling loss in the Y-junction or directional coupler, and loss due to biasing the modulator. Losses are typically in the 3 to 10 dB range

A $V_\pi L$ of 0.035 V-cm has been demonstrated in a silicon modulator at 10 Gb/s by using electrical pre-emphasis [28]. 50 Gb/s silicon modulators have been fabricated with a reported $V_\pi L$ of 1.1 V-cm [29]. In Lithium Niobate, a range of modulators from 70 GHz and 5.1 Vπ [30] to 30 MHz and 0.18 Vπ [31] has been reported.

2.6 Fabrication

Details of the fabrication of this device have been previously published in [32]-[34]. Fabrication occurred at the Institute of Microelectronics (IME)/ASTAR [35],[36]. The starting material was an 8” Silicon-on-Insulator wafer from SOITEC, with a Boron-doped top silicon layer of around 10 ohm-cm resistivity and 220 nm thickness, a 2 μm bottom oxide thickness, and a 750 ohm·cm handle silicon wafer, needed for RF performance. A 60 nm anisotropic dry etch was first applied to form the trenches of the grating couplers. Next, the rib waveguides for the modulator were formed using additional etch steps. In all cases 248 nm photolithography was utilized. The p++, p, n++, and n implants for the modulator were performed on the exposed silicon, prior to any oxide fill. This was followed by a rapid thermal anneal at 1030 ºC for 5 s for Si dopant activation. It was followed by the formation of contact vias and two levels of aluminum interconnects. Chemical-mechanical planarization was not utilized. The schematic cross-section is shown in Figure 5.

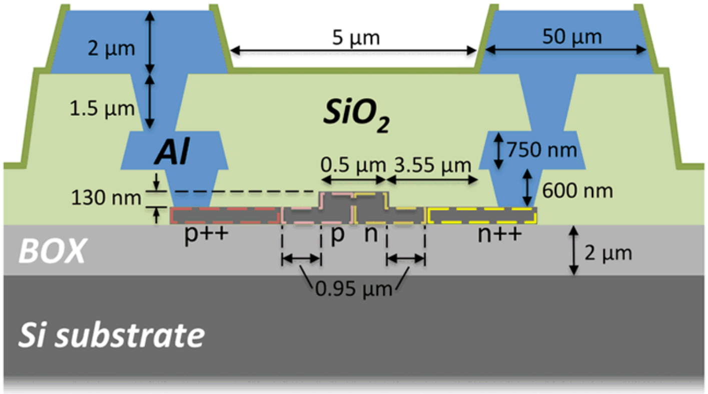

Figure 5. A cross-section of the fabricated device is shown, with the two metal layers indicated, as well as the rib waveguide structure and the lateral pn junction.

Chapter 3 Intermodulation and Harmonic Distortion

This chapter discusses the mathematics and theory of intermodulation and harmonic distortion in a traveling wave modulator, as well as methods of modeling these distortions.

3.1 Theory

A linear time invariant system can be said to have transfer function $H(j\omega)$. Subject to input $X(j\omega)$, the system output is described as $Y(j\omega) = H(j\omega)X(j\omega)$. However, in the presence of nonlinearities, the transfer function may no longer be described as a simple dependence of input frequency. Instead, the output function may be described as a general function of the input, x(t), denoted here as $Y(x)$. The Taylor series expansion of $Y(x)$ about $x = a$ may be represented as:

$$Y(x) = \sum_{n=0}^{\infty} c_n x^n = c_0 + c_1(x-a) + c_2(x-a)^2 + c_3(x-a)^3 + \cdots \tag{9}$$

where:

$$c_n = \frac{1}{n!}\left(\frac{d^nY}{dx^n}\right)_{x=a}$$

For sinusoidal inputs $x(t) = \sin(2\pi ft)$, the Taylor expansion shown in (9) about $x = 0$, becomes:

$$Y(x) = \sum_{n=0}^{\infty} c_n \sin^{\mathrm{n}}(2\pi ft) \tag{10}$$

$$= c_0 + c_1 \sin(2\pi ft) + c_2 \sin^2(2\pi ft) + c_3 \sin^3(2\pi ft) + \cdots$$

From the double-angle trigonometric identity, (10) may be rewritten:

$$Y(x) = c_0 + c_1 \sin(2\pi f t) + \frac{c_2}{2}\sin(4\pi f t) + \frac{c_3}{4}\sin(6\pi f t) + \cdots \tag{11}$$

Thus, it can be shown that harmonic distortion and intermodulation distortion may create output frequency components at frequencies other than those of the input. Often times for a single input frequency, the third order nonlinearity is far outside the pass band of the system. However, if two in-band sinusoids of near but distinct frequencies are present, the third order effect will create an additional term that is also in-band. For example, consider a double sideband suppressed carrier wave represented as:

$$x(t) = \mathrm{a}_1\cos(2\pi f_1 t) + \mathrm{a}_2\cos(2\pi f_2 t) \tag{12}$$

The $n = 2$ term from (10) is expanded:

$$c_2 x^2 = c_2(\mathrm{a}_1\cos(2\pi f_1 t) + \mathrm{a}_2\cos(2\pi f_2 t))^2$$

$$\Rightarrow \left[\frac{c_2 a_1^2}{2} + \frac{c_2 a_2^2}{2}\right] + \frac{c_2 a_1^2}{2}\cos(4\pi f_1 t) + \frac{c_2 a_2^2}{2}\cos(4\pi f_2 t) \tag{13}$$

$$+ c_2 a_1 a_2 \cos(2\pi(f_1 + f_2)t)$$

And, similarly, the $n = 3$ term from (10) is expanded:

$$c_3 x^3 = c_2(\mathrm{a}_1\cos(2\pi f_1 t) + \mathrm{a}_2\cos(2\pi f_2 t))^3$$

$$\Rightarrow \left[\frac{3c_3a_1^3}{4} + \frac{3a_1a_2^2}{2}\right]\cos(2\pi f_1 t) + \left[\frac{3c_3a_2^3}{4} + \frac{3a_2a_1^2}{2}\right]\cos(2\pi f_2 t)$$
$$+ \frac{c_3a_1^3}{2}\cos(6\pi f_1 t) + \frac{c_3a_2^3}{2}\cos(6\pi f_2 t)$$
$$+ \frac{3c_3a_1a_2^2}{4}\left(\cos\left((2(2\pi f_1) + 2\pi f_2)t\right)\right.$$
$$\left.+ \cos\left((2(2\pi f_1) - 2\pi f_2)t\right)\right) \tag{14}$$
$$+ \frac{3c_3a_2a_1^2}{4}\left(\cos\left((2(2\pi f_2) + 2\pi f_1)t\right)\right.$$
$$\left.+ \cos\left((2(2\pi f_2) - 2\pi f_1)t\right)\right)$$

The frequency doubling effect in the $n = 2$ term is known as harmonic distortion. For the $n = 3$ expansion, the additional in-band sinusoidal terms at $2f_2 - f_1$ and $2f_1 - f_2$ are known as intermodulation distortion. Here, we are ignoring terms for $n > 3$; we assume that these higher order effects are sufficiently attenuated.

Representing the carrier wave input in (12) as a sum and difference of frequency f_m on a principal frequency f_c:

$$x(t) = \mathrm{a}_1\cos(2\pi(f_c + f_m)\,t) + \mathrm{a}_2\cos(2\pi(f_c - f_m)\,t) \tag{15}$$

Thus, it is shown that intermodulation distortion results in additional output sinusoids at frequencies:

$$f = f_c \pm nf_n \tag{16}$$

while harmonic distortion results in output frequencies at:

$$f = mf_c \pm nf_n \tag{17}$$

3.2 Mach-Zehnder Transfer Function Nonlinearities

The transfer function and its first three derivatives of a Mach-Zehnder modulator biased at quadrature are:

$$I_{out} = \frac{GI_{in}}{2}(1 + \sin(\phi)) \tag{18}$$

$$\frac{dI_{out}}{dV} = \frac{GI_{in}}{2}\cos(\phi)\,\phi' \tag{19}$$

$$\frac{d^2I_{out}}{dV^2} = \frac{GI_{in}}{2}[-\sin(\phi)\,\phi'^2 + \cos(\phi)\,\phi''] \tag{20}$$

$$\frac{d^3I_{out}}{dV^3} = \frac{GI_{in}}{2}[-\cos(\phi)\,\phi'^3 - 2\sin(\phi)\,\phi'\phi'' - \sin(\phi)\,\phi'\phi'' + \cos\,(\phi)\phi'''] \tag{21}$$

Where ϕ is the phase vs. voltage relationship of the modulator and is a nonlinear a function of voltage V, I_{in} is the intensity of input light, and G is the optical insertion loss of the modulator.

From the previous section, it can be shown that the harmonic distortion in the optical signal is defined as:

$$SHD = \frac{1}{2!}\frac{d^2I_{out}}{dV^2}\bigg|_{V=0}\frac{1}{2}V_0^2\cos(2\omega t) \tag{22}$$

For input $V = V_0\cos(\omega_1 t) + V_0\cos\,(\omega_2 t)$, the intermodulation product for the optical signal is:

$$IMD_3 = \frac{1}{3!}\frac{d^3I_{out}}{dV^3}\bigg|_{V=0}\frac{3}{4}V_0^3\cos(2\omega_2 t - \omega_1 t) \tag{23}$$

To obtain a prediction for the SFDR measured at a spectrum analyzer after a photodetector, one may use the following conversion from optical power into electrical power in dBm:

$$P_{sig} = 10\log\left(\frac{(P_{recv}\sigma)^2}{1000 \cdot R}\right) \tag{24}$$

where P_{recv} is the optical power at the photodetector, σ is the response of the photodetector in Volts/Watt, and R is the impedance of the receiving electronics.

Chapter 4 Experimental Results

The Mach-Zehnder modulator studied in this work was tested for DC and RF performance, in addition to spur-free dynamic range. A small-signal Vπ of 5.6 V and 6.2 V for the top and bottom arms, respectively, and 6.2 dB of optical insertion loss was measured, as well as a 15.5 GHz bandwidth. An SFDR as high as 104.5 $\mathrm{dB{\cdot}Hz^{2/3}}$ is measured.

4.1 DC and RF characterization

Some of the important parameters to know about the modulator are: insertion loss, V_π, and 3 dB bandwidth. The first two performance metrics, V_π and insertion loss, may be measured in the same way that one would measure a phase shifter, mentioned earlier. For a device utilizing differential drive—where complementary signals are applied to each arm of the Mach-Zehnder—bandwidth may be tested one arm at a time.

Additionally, for testing or other purposes, it is often useful to unbalance the Mach-Zehnder to create fringing in the transmission spectrum. In this way, the bias of the modulator may be tuned by changing the wavelength of the light source. This is often desired over simply changing the bias of the drive voltage due to the nonlinear change in n_{eff} vs. voltage—at higher biases there is reduced modulation. An example of this fringing is shown below for a 100 μm unbalance in a 3 mm long device:

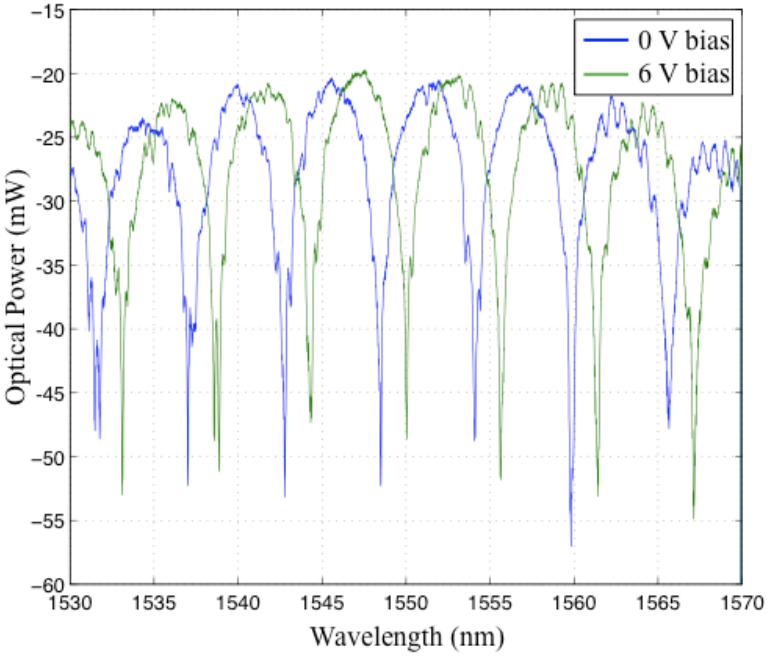

Figure 6. Optical transmission versus wavelength at different reverse bias conditions

Varying the bias condition for the modulator and observing the shift in transmission reveals the following phase shift versus voltage dependence:

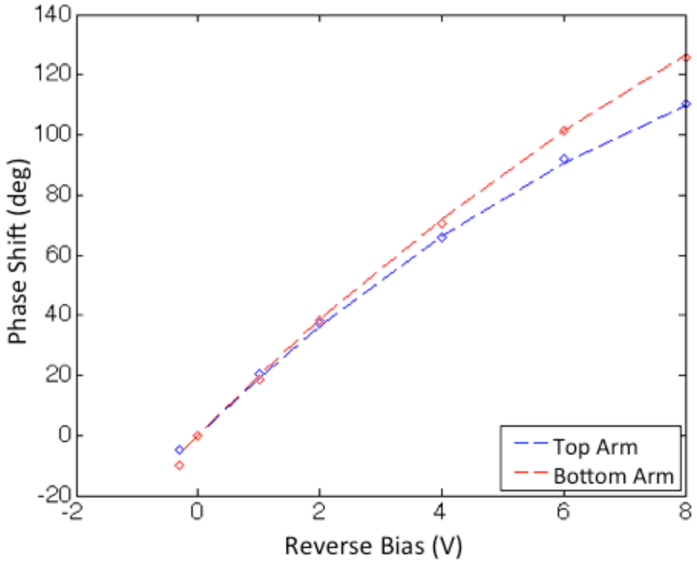

Figure 7. Phase shift of the optical mode versus reverse bias for each arm of the Mach-Zehnder modulator.

From Figure 7, the nonlinearity of the phase shifter is clearly demonstrated. Additionally, each arm has a distinct nonlinearity. Fiting the above plot with the following function:

$$\phi = bV + cV^2 + dV^3 \tag{25}$$

Will obtain the following fit parameters:

Table 1. Fit parameters for phse shift versus reverse bias voltage

MZM arm	b (rad/V)	c (rad/V^2)	d (rad/V^3)
Bottom	0.352	0.0167	3.49×10^{-4}
Top	0.361	-0.0126	2.50×10^{-4}

Based on the fit of the phase shift versus junction bias at a 0 V bias, the model predicts a 2nd order limited $\mathrm{SFDR_{SHD}}$ of 87 dB·$\mathrm{Hz}^{1/2}$ for a differentially driven MZ and 75 dB·$\mathrm{Hz}^{1/2}$ when driving only a single arm. The gain achieved by differential drive for second harmonic distortion is limited by the relative pn-junction performance of each arm. Since the top and bottom arms exhibit different nonlinearities, biasing the modulator at quadrature does not cancel the second order term as it does for a linear electrooptic effect modulator. This model also predicts an $\mathrm{SFDR_{IMD}}$ of 94 dB·$\mathrm{Hz}^{2/3}$ and 98 db·$\mathrm{Hz}^{2/3}$ for the single arm and differential drive cases, respectively. In this case, the third order SFDR is expected to improve by 4 dB not due to cancellation of the third order terms from the pn-junction nonlinearity, but because differential drive effectively increases the output powers of the fundamental and distortion terms by 6 dB.

During all RF testing, care was taken to properly terminate each arm of the modulator. Each a 33 Ω transmission line is driven by a 50 Ω impedance GSG probe and terminated with two 50 Ω terminators in parallel from a GSSG probe. In this case, since the reflections between a 33 Ω line and 50 Ω or 25 Ω are fairly small, either termination scheme would have realistically worked for both pads. For differential drive testing, GSGSG and GSSGSSG probes are used.

Figure 8. Termination pad configuration for the Mach-Zehnder Modulator

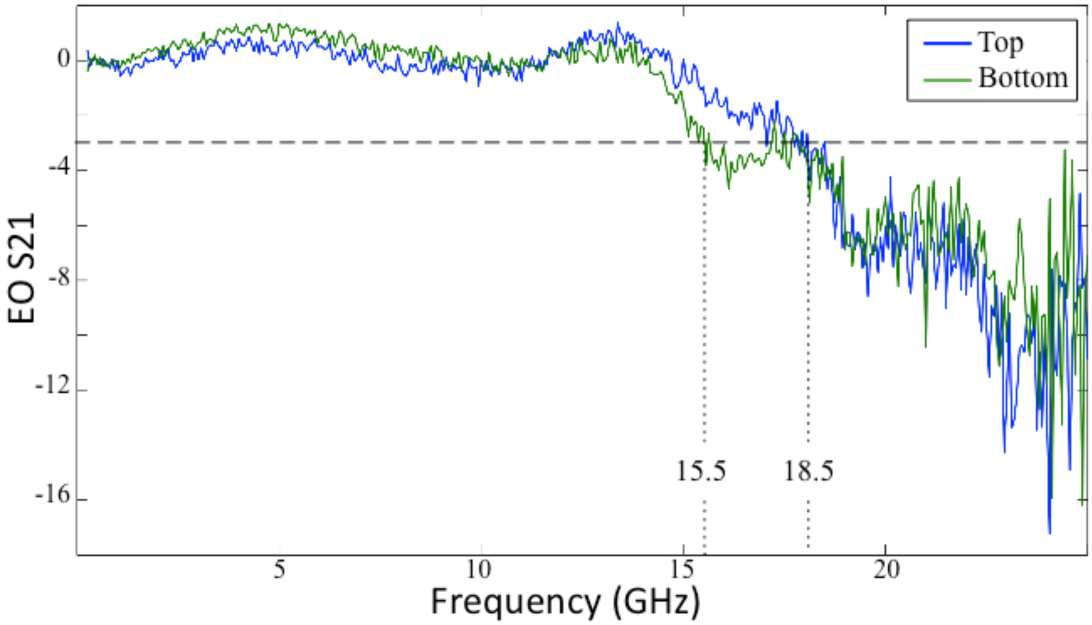

Figure 9. Measured bandwidth for the top and bottom arms of the Mach-Zehnder modulator

4.2 Linearity measurements

A tunable laser light source is input into an erbium-doped fiber amplifier and then through a polarization rotator. The polarized light is coupled into the modulator from an optical fiber with a grating coupler holographic lens and routing waveguides. The modulated signal is coupled back into an optical fiber with another grating coupler. Each grating coupler has a known 4.4 ± 0.2 dB loss and the waveguides have 2.2 ± 0.8 dB/cm loss. To achieve quadrature, the wavelength of input light is adjusted to the -3 dB point in the spectrum. The principal limiting factor of this test was the photodetector saturation power of 2 mW.

The experimental setup is shown in Fig. 4. An arbitrary waveform generator (AWG) and a vector network analyzer (VNA) are used as signal sources. The AWG is capable of producing complementary signals, while the VNA is not. To create a complementary signal, the VNA output is passed through a splitter and recombined after delaying one path with close to three inches of additional rf cabling. The frequency of modulation was adjusted to tune the phase difference and achieve complementary signals. The data for this calibration is shown below:

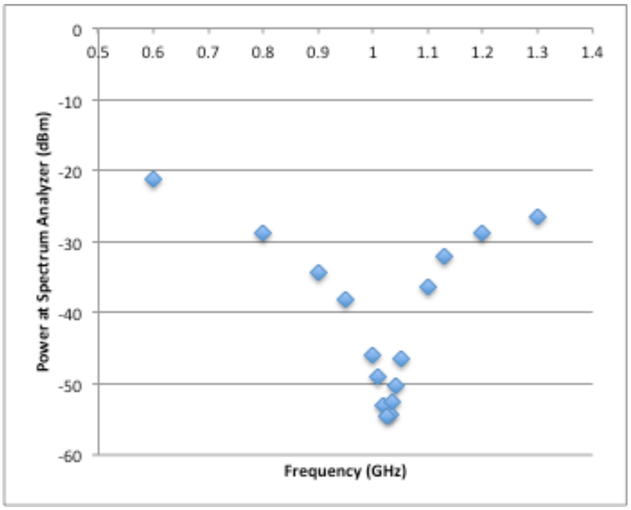

Figure 10. Frequency calibration for rf path length difference in order to achieve out of complementary signals

Two signals near 1 GHz were applied to the MZM. In principle, higher bandwidth signals could be used but is limited here by the detection bandwidth of the spectrum analyzer.

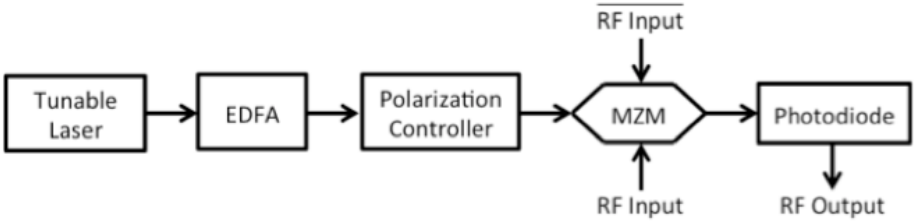

Figure 11. Block diagram of experimental setup for SFDR measurements

A typical RF spectra of intermodulation distortion is presented in Figure 12. The nonlinearity of the MZM driven by a single arm is presented in Figure 13 and the nonlinearity of the differentially driven MZM is shown in Figure 14. The EDFA amplified the tunable laser to about 500 mW and 1 mW of light is received at the photodetector. The photodetector produces an output of 15 V/W.

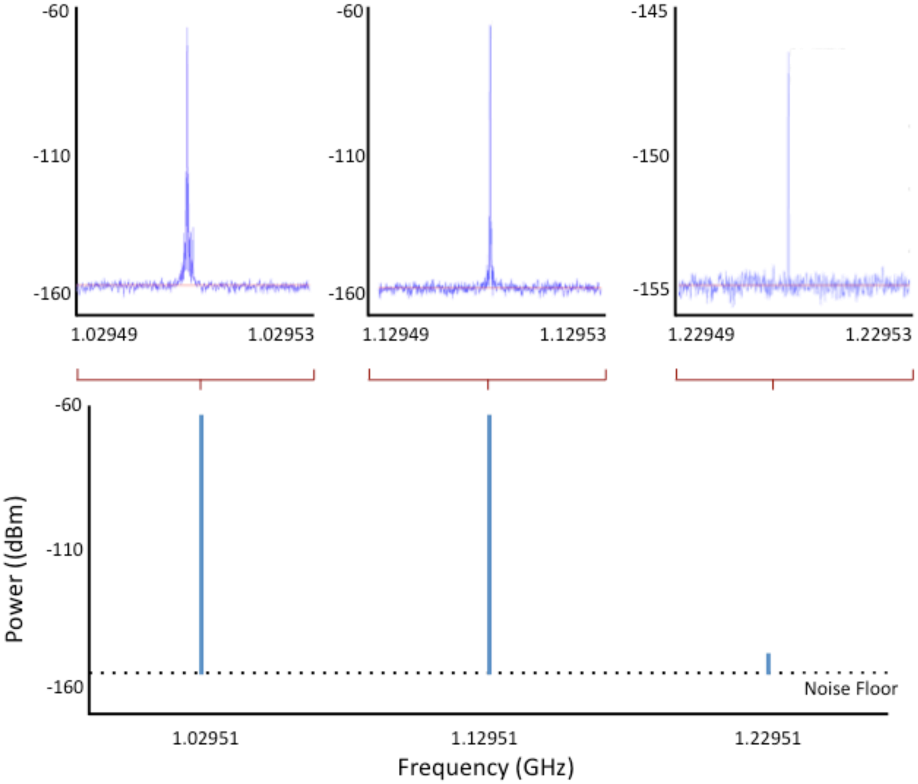

Figure 12. Example reconstructed RF spectrum showing the fundamental tones at 1.02951 and 1.12951 GHz and the intermodulation distortion at 1.22951 GHz

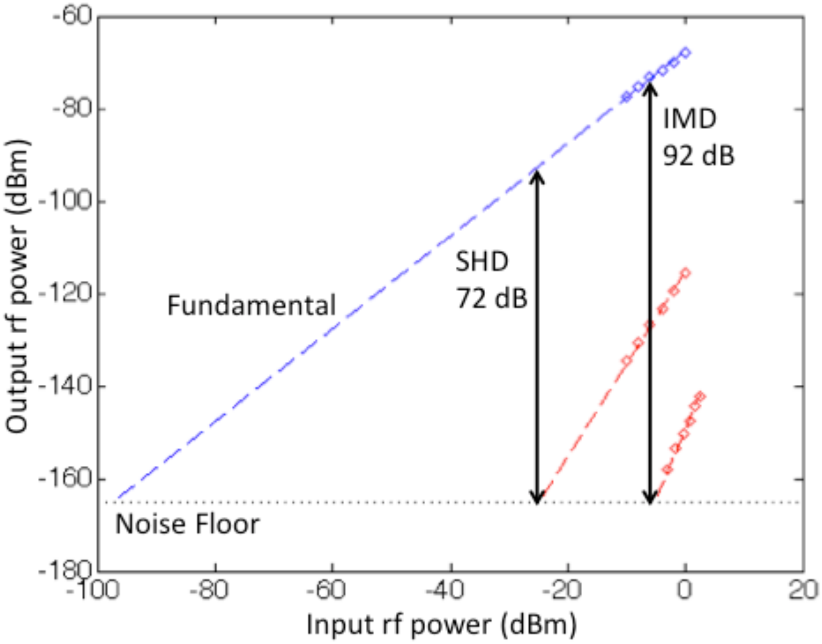

Figure 13. Output power vs. input power of the second harmonic distortion and intermodulation distortion for an MZM driven by a single arm. Spur-free dynamic ranges of 72 dB·Hz$^{1/2}$ and 92 dB·Hz$^{2/3}$ are measured for SFDR$_{SHD}$ and SFDR$_{IMD}$, respectively.

A Noise Floor of -165 dBm/Hz was observed and is used to calculate SFDR. SFDR$_{SHD}$ and SFDR$_{IMD}$ for the single arm case at 0 V bias are found to be 72 dB·Hz$^{1/2}$ and 92 dB·Hz$^{2/3}$, respectively. By differentially driving the modulator the SFDR is found to increase to 82 dB·Hz$^{1/2}$ and 97 dB·Hz$^{2/3}$ for SFDR$_{SHD}$ and SFDR$_{IMD}$, respectively. For both single arm and differential drive operation, these values are within 3 dB of our predicted values based on the nonlinearity of the pn junction. This suggests that the junction is the dominant nonlinearity for this system.

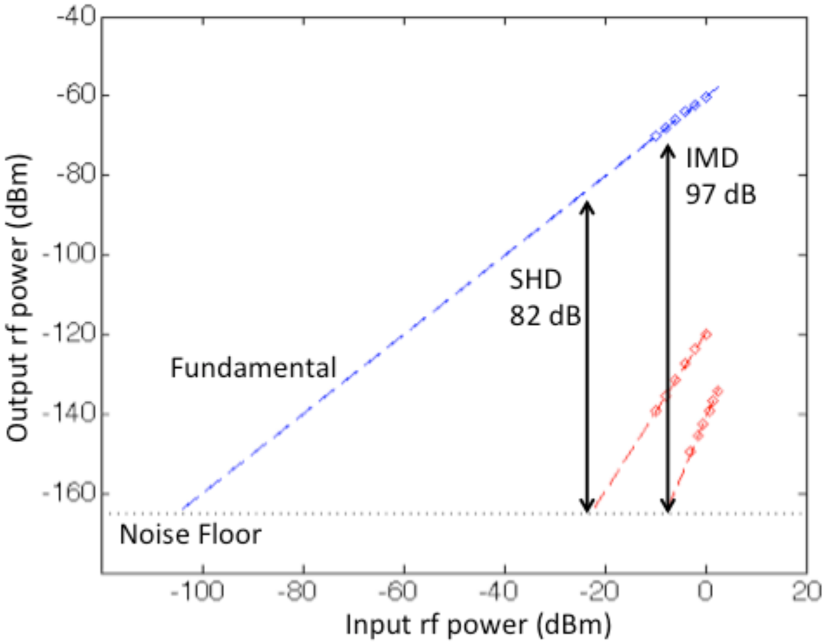

Figure 14. Output power vs. input power of the second harmonic distortion and intermodulation distortion for a differentially driven MZM. Spur-free dynamic ranges of 82 dB·Hz$^{1/2}$ and 97 dB·Hz$^{2/3}$ are measured for SFDR$_{SHD}$ and SFDR$_{IMD}$, respectively.

Additionally, since there is a known optical loss after the device, the SFDR of the MZM is greater than what is measured. After the output of the MZM, there is 1.2 dB of loss in the routing waveguides, and 6.3 dB of net loss under testing conditions due to the grating coupler. One cannot generally normalize out optical losses from an SFDR calculation, since this neglects the possible power-handling limitations of the devices. However, known losses that occur after the device can certainly be removed with improved engineering efforts, without affecting the power that flows through the device. As a result, we predict that the on-chip 3rd order limited SFDR would be 104.5 dB·Hz$^{2/3}$ and the 2nd order limited SFDR should be 89.5 dB·Hz$^{1/2}$, if one removes only the coupling losses that occur after the Mach-Zehnder.

Note that only 50 mW of optical power enters the input waveguides of the MZM, which is well below the power saturation limit of typical silicon photonics devices with these dimensions [21]. Presumably, the SFDR could be further improved by increasing the optical power in the device, through either a more powerful input optical signal, or lower coupling losses. We note that the propagating power in the results described in [16,17] was on the order of 500 mW and 240 mW, respectively. Based on our results, we believe that silicon-based Mach-Zehnder modulators could become important tools for future analog applications in integrated optics.

Chapter 5 Future Work

5.1 Linearized Mach-Zehnder Modulators

As mentioned in previous sections, the marginal cost of complexity for optical devices in silicon allows for the implementation of complex linearization schemes. There are several such linearization techniques that have been proposed and tested successfully in other material systems. The first four methods described here (ring assisted modulators, cascaded modulators, carrier suppression, and electrical precompensation) directly compensate for the nonlinear transfer function of the Mach-Zehnder modulator. However, there has not yet been any published work on how to directly compensate for the pn junction nonlinearity in Mach Zehnder modulators. Khilo et al. suggest that by biasing the modulator at quadrature the second order nonlinearity should cancel if the two arms are balanced [37]. This, in principle, should be possible though will require much more careful control of the processing in future iterations of the Mach-Zehnder tested in this work. Nevertheless, these methods are worth exploring in future works.

5.1.1 Ring Assisted Modulators

By placing a microring resonator near the arm of a Mach-Zehnder modulator, the modulation efficiency and linearity may both improve. A schematic of what such a device might look like is shown below in Figure 15.

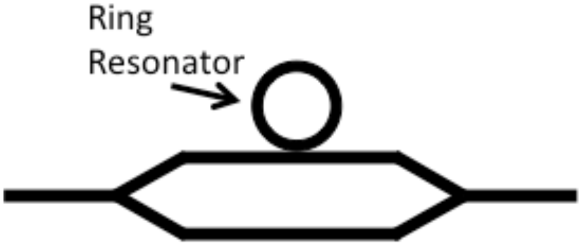

Figure 15. Diagram of a ring assisted Mach-Zehnder modulator.

There have been several such designs implemented in silicon already [38]-[40]. Most recently, Guiterrez *et al.* demonstrated a 19 GHz bandwidth ring assisted silicon modulator with an interaction length of 200 µm [41]. In their work in silicon, these authors do not measure the nonlinearities of the modulator. However, the SFDR has been measured in other material systems. For example, in [42], Yang et al. analyze the different effects of ring performance and design on the linearity of such a modulator. Plotted in Figure 16 is the transfer function of a ring assisted modulator versus bias condition on one arm. On visual inspection of the transfer function of the modulator with it's unmodified counterpart, the increase in linearity is very readily observed. At the proper bias, the linear region is significantly stretched beyond the sinusoidal transfer function of non-assisted modulators. For linear electrooptic effect modulators, SFDR improvements by as much as 20 dB are possible through this technique [43].

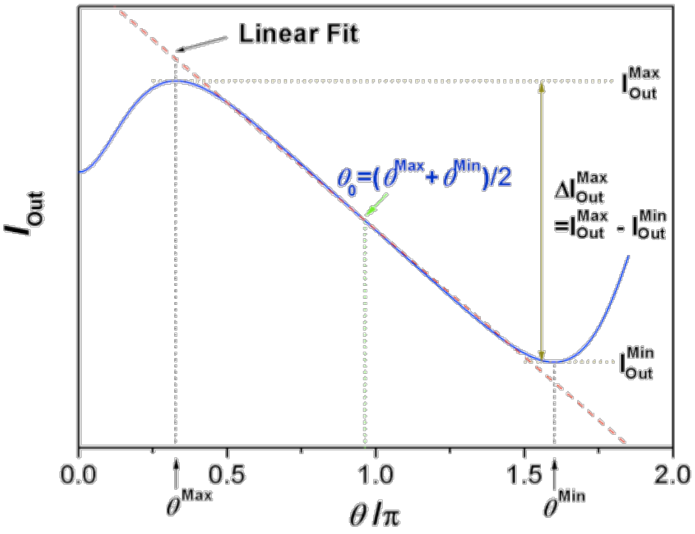

Figure 16. Transfer function of a ring assisted Mach-Zehnder modulator fabricated in Lithium Niobate. Plot is from [42].

5.1.2 Cascaded Modulators

In addition to ring assisted modulators, there has also been significant investigation into cascading optical modulators [45]-[47]. However, unlike the broadband ring assisted modulators, cascaded modulators are often operated in a sub-octave bandwidth or otherwise may be dominated by second order distortion [44]. Several topographies are reviewed by Ackerman and shown in Figure 17.

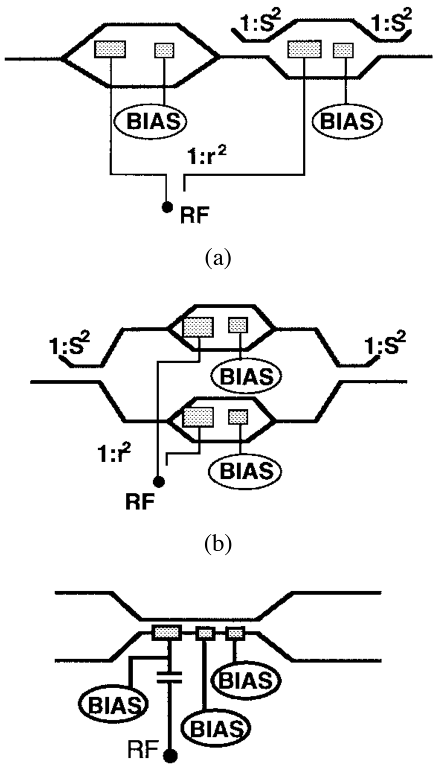

(a)

(b)

Figure 17. Three topographies for cascaded interferometer-based optical modulators. Figure from [44].

The largest SFDR reported with a sub-octave linearized modulator is 134 $\mathrm{dB \cdot Hz^{2/3}}$ at 150 MHz [48]. There is no fundamental problem with cascaded modulators that prevents devices from reaching faster speeds. However, many of these designs are limited by practical concerns such as requiring careful RF design and high manufacturing tolerances.

5.1.3 Carrier Suppression

In addition to different modulator topographies, optical filtering may also be used to linearize the transfer function of a Mach Zehnder modulator. Taking the fourier transform of the Mach-Zehnder modulator transfer function:

$$I_{out} = \frac{I_0}{2}\left[1+\cos(2Z(t)+\varphi)\right] \tag{26}$$

one obtains:

$$I_{out} = \cos\left(\frac{\varphi}{2}\right) \sum_{even\ k=-\infty}^{\infty} J_k\left(\frac{\pi}{V_\pi}A\right) e^{jk\omega t+\theta} + j\sin\left(\frac{\varphi}{2}\right) \sum_{odd\ k=-\infty}^{\infty} J_k\left(\frac{\pi}{V_\pi}A\right) e^{jk\omega t+\theta} \tag{27}$$

From (27), it is clear that the transfer function consists of a main carrier and sidebands. By placing an optical filter directly after the modulator, it is possible to filter for only the desired sideband, typically the first. An outline of this process is diagrammed in Figure 18.

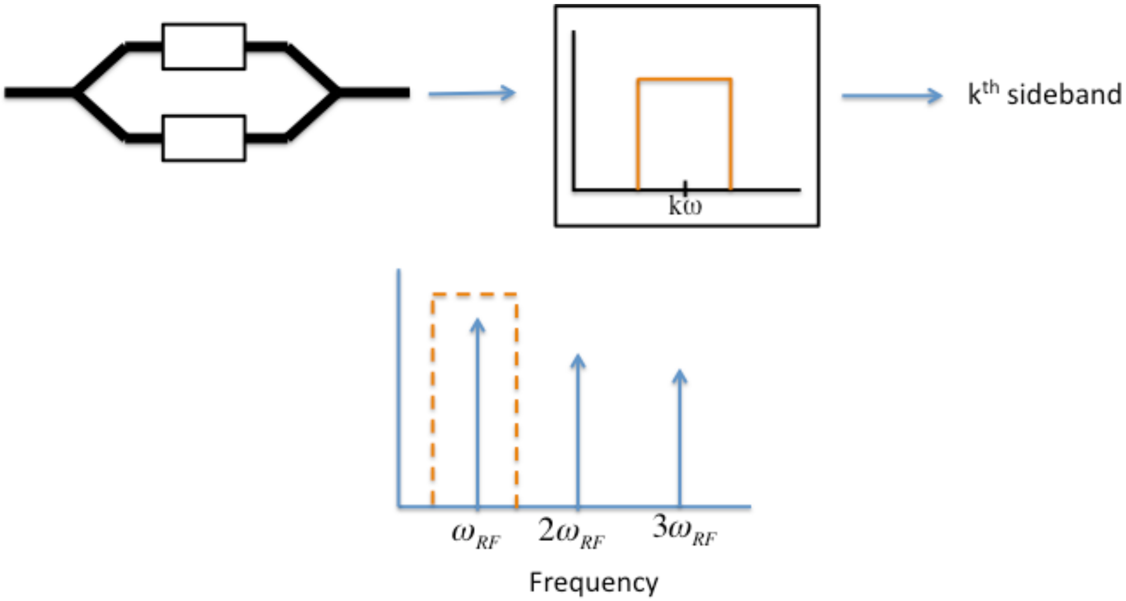

Figure 18. Overview of carrier suppression to select the desired sideband in the transfer function of a Mach-Zehnder modulator.

Tu *et al*. have fabricated an optical filter in silicon suitable for such a purpose. In their paper, they couple an external Lithium Niobate Mach-Zehnder modulator to the silicon optical filter and achieve an 11 dB gain in SFDR [49]. It should be theoretically possible to integrate a variation of this filter onto the same silicon substrate as the modulator presented here.

5.1.4 Electrical Precompensation

It is also possible to use electrical methods to linearize the transfer function. Essentially, the goal is to apply the inverse of the nonlinearity to the driving electrical signal to compensate for any distortion the modulator would introduce. A block diagram illustrating this is presented in Figure 19.

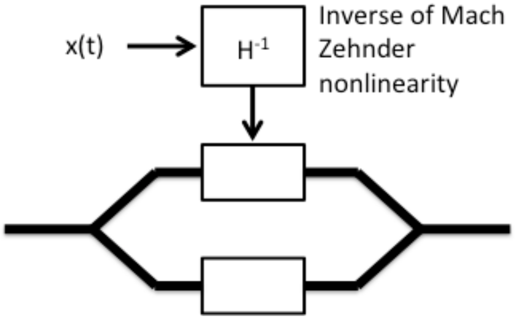

Figure 19. Block diagram of electrical precompensation

This design has been implemented in a variety of schemes. By using a CMOS predistortion circuit Sadhwani and Jalali improved the SFDR of an external Mach Zehnder modulator by 6 dB [50]. In the purely analog domain, Agarwal *et al*. used a coherent detection scheme and a second Mach-Zehnder modulator to improve SFDR by 13 dB [51]. With coherent detection, it was shown that the functional form to compensate for the distortion was significantly simpler than in the intensity modulated direct detection case.

5.1.5 Varied junction designs

To directly tackle the nonlinearity of the pn-junction, other junction designs could also be considered. In fact, Lo *et al*. found that, based on simulation results, the nonlinearities introduced by a p-i-p-i-n junction actually serve to cancel the nonlinearities in the Mach-Zehnder transfer function [19]. There have also been several successful uses of a p-i-p-i-n junction in silicon Mach-Zehnder modulators. Most recently, Ziebell *et al.* demonstrated a 40 Gbit/s modulator, with cross section shown in Figure 20 [52].

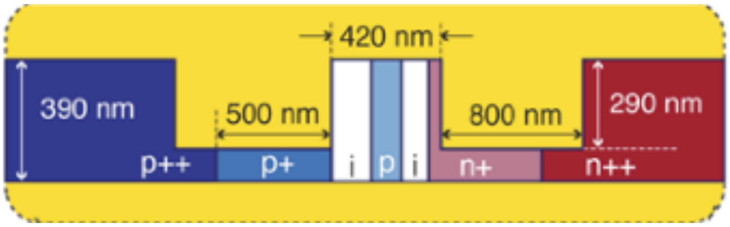

Figure 20. Example doping profile of a p-i-p-i-n modulator. Figure from [52].

Bibliography

[1] Miller, S.E., *Integrated optics: an Introduction.* B.S.T.J., 1969. 48(7): p. 2059-2069.

[2] R. Soref, A. Bennett, “Electrooptical Effects in Silicon”. *IEEE Journal of Quantum Electronics* 23 (1): 123-129. Doi: 10.1109/JQE.1987.1073206

[3] T. Baehr-Jones, T. Pinguet, P. Lo Guo-Qiang, S. Danziger, D. Prather and M. Hochberg, “Myths and Rumors of Silicon Photonics,” *Nature Photonics* 6, 206-208 (2012).

[4] Kaminow, Ivan P, Tingye Li, *Optical Fiber Telecommunications IV, Vol. I*, Elsevier Press, 2002.

[5] R. Soref, “The past, present and future of silicon photonics,” *IEEE J. Sel. Top. Quantum Electron* 12(6), 1678–1687 (2006).

[6] B. Jalali and S. Fathpour, “Silicon photonics,” *J. Lightwave Technol*. 24(12), 4600–4615 (2006).

[7] R. A. Minasian, “Photonic signal processing of microwave signals,” *IEEE Trans. Microw. Theory Tech*. 54(2), 832–846 (2006).

[8] A. Liu, R. Jones, L. Liao, D. Samara-Rubio, D. Rubin, O. Cohen, R. Nicolaescu, and M. Paniccia, “A high-speed silicon optical modulator based on a metal-oxide-semiconductor capacitor,” *Nature*, vol. 427, pp. 615–618, Feb. 2004.

[9] S.J.Spector,M.W.Geis,G.-R.Zhou,M.E.Grein,F.Gan,M.A.Popovic´, J. U. Yoon, D. M. Lennon, E. P. Ippen, F. X. Ka¨rtner, and T. M. Lyszczarz, “CMOS-compatible dual-output silicon modulator for analog signal processing,” *Opt. Exp*., vol. 16, no. 15, pp. 11027–11031, Jul. 2008.

[10] T. Baehr-Jones, R. Ding, Y. Liu, A. Ayazi, T. Pinguet, N. C. Harris, M. Streshinsky, P. Lee, Y. Zhang, A. Eu-Jin Lim, T. Y. Liow, S. H. G. Teo, G. Q. Lo, and M. Hochberg, "Ultralow drive voltage silicon traveling wave modulator," *Opt. Exp*. 20, 12014-12020 (2012).

[11] T. Ismail, C.-P. Liu, J. E. Mitchell, and A. J. Seeds, "High-dynamic- range wireless-over-fiber link using feed forward linearization," *J. Lightwave Technol.* vol. 25 no. 11, pp. 3274–3282 (2007).

[12] C. H. Cox III, E. I. Ackerman, G. E. Betts, and J. L. Prince, "Limits on the performance of RF-over-fiber links and their impact on device design," *IEEE Trans. Microw. Theory Tech.*, vol. 54, no. 2, pp. 906–920, Feb. 2006.

[13] J. C. Fan, C. L. Lu, and L. G. Kazovsky, "Dynamic range requirements for microcellular personal communication systems using analog fiber-optic links," *IEEE Trans. Microw. Theory Tech*., vol. 45, pp. 1390–1397, Aug. 1997.

[14] W. B. Bridges and J. H. Schaffner, "Distortion in linearized electrooptic modulators," *IEEE Trans. Microw. Theory Tech*. 43(9), 2184–2197 (1995).

[15] E. I. Ackerman, A.S. Daryoush, "Broad-band external modulation fiber-optic links for antenna-remoting applications," *IEEE Trans. Microw. Theory Tech*., vol. 45, no. 8, pp. 1436-1442, Feb. 1997.

[16] S. Dubovitsky, W. H. Steier, S. Yegnanarayanan, and B. Jalali, "Analysis and improvement of Mach-Zehnder modulator linearity performance for chirped and tunable optical carriers," *J. Lightw Technol*. 20(5), 886–891 (2002).

[17] M. Sauer, A. Kobyakov, and J. Geoge, “Radio Over Fiber for Picocellular Network Architectures,” *IEEE J. Lightwave Technol*. Vol. 25, no. 11, pp. 3301-3320 (2007).

[18] A. Ayazi, T. Baehr-Jones, Y. Liu, A. E.-J. Lim, and M. Hochberg, “Linearity of silicon ring modulators for analog optical links,” *Opt. Exp*. 20, 13115-13122 (2012).

[19] S. Lo, C. Li, H.K. Tsang, “Linearity of Carrier Depletion based Silicon Optical Modulators,” 15th Optoelectronics and Communications Conference Technical Digest, July 2010

[20] A. Karim, J. Devenport, “Noise Figure Reduction in Externally Modulated Analog Fiber-Optic Links*,” IEEE Photon. Technol. Lett.* Vol.19 No.5 March 2007.

[21] K. J. Williams, L. T. Nichols, R. D. Esman, “Photodetector Nonlinearity Limitations on a High-Dynamic Range 3 GHz Fiber Optic Link,” *J. Lightw. Technol*., Vol. 16, No. 2, February 1998.

[22] B. Liu, J. Shim, Y. Chiu, A. Keating, J. Piprek, and J. Bowers, “Analog characterization of low-voltage MQW traveling-wave electroabsorption modulators,” *J. Lightw. Technol.,* vol. 21, no. 12, pp. 3011–3019, Dec. 2003.

[23] H. Haug and S. W. Koch, *Quantum Theory of the Optical and Electronic Properties of Semiconductors*, World Scientific, 1994

[24] J. I. Pankove, *Optical Processes in Semiconductors,* Dover (1971)

[25] Kip, Arthur F. *Fundamentals of Electricity and Magnetism*. McGraw-Hill, 1969

[26] Thomson, D.J.; Gardes, F.Y.; Fedeli, J.-M.; Zlatanovic, S.; Youfang Hu; Kuo, B.P.P.; Myslivets, E.; Alic, N.; Radic, S.; Mashanovich, G.Z.; Reed, G.T.; , "50-

Gb/s Silicon Optical Modulator," *Photonics Technology Letters, IEEE* , vol.24, no.4, pp.234-236, Feb.15, 2012

[27] Y. Liu, "Enhanced Optical Modulation in Integrated Silicon Waveguides for the Near-Infrared," M.S. Thesis, E.E., U.W., Seattle, WA, 2012

[28] W. M. J. Green, J. M. Rooks, L. Sekaric, and Y. A. Vlasov, "Ultra-compact, low RF power, 10 Gb/s silicon Mach-Zehnder modulator," *Opt. Express* **15**, 17106-17113 (2007).

[29] M. R. Watts, W. A. Zortman, D. C. Trotter, R. W. Young, and A. L. Lentine, "Low-voltage, compact, depletion-mode, silicon Mach-Zehnder modulator," *IEEE J. Sel. Topics Quantum Electron*. **16**, 159-164 (2010).

[30] K. Noguchi, O. Mitomi, and H. Miyazawa, "Millimeter-wave Ti LiNbO optical modulators," *J. Lightw. Technol.*, vol. 16, no. 4, pp. 615–619, Apr. 1998.

[31] G. Betts, L. Johnson, and C. Cox, "High-sensitivity lumped-element bandpass modulators in LiNbO ," *J. Lightw. Technol.*, vol. 7, no. 12, pp. 2078–2083, Dec. 1989.

[32] T. Baehr-Jones, R. Ding, A. Ayazi, T. Pinguet, M. Streshinsky, N. Harris, J. Li, L. He, M. Gould, Y. Zhang, A. E.-J. Lim, T.-Y. Liow, S. H.-G. Teo, G. Qiang Lo, and M. Hochberg, "A 25 Gb/s Silicon Photonics Platform," *IEEE Micro*. 2012 (In Review)

[33] Tom Baehr-Jones, Ran Ding, Yang Liu, Ali Ayazi, Thierry Pinguet, Nicholas C. Harris, M. Streshinsky, Poshen Lee, Yi Zhang, Andy Eu-Jin Lim, Tsung-Yang Liow, Selin Hwee-Gee Teo, Guo-Qiang Lo, and Michael Hochberg, "Ultralow drive voltage silicon traveling-wave modulator." *Opt. Express* (In Press)

[34] M. Streshinsky, A. Ayazi, Z. Xue, A. Eu-Jin Lim, G. Qiang Lo, T. Baehr-Jones, M. Hochberg, "Linearity of Differentially Driven Travelling Wave Mach-Zehnder Silicon Carrier Depletion Modulators," *IEEE Microw. Theory and Tech*. 2012

[35] http://www.ime.a-star.edu.sg/PPSSite/index.asp.

[36] T-Y. Liow, K-W. Ang, Q. Fang, J-F. Song, Y-Z. Xiong, M-B. Yu, G-Q. Lo, and D-L. Kwong, "Silicon modulators and germanium photodetectors on SOI: monolithic integration, compatibility, and performance optimization," *IEEE J. Sel. Top. Quantum Electron.* 16, 307-315 (2010).

[37] A. Khilo, C. M. Sorace, F. X. Kärtner, "Broadband linearized silicon modulator," *Op. Ex.*, Vo. 19 No. 5, 2011

[38] D. M. Gill, S. S. Patel, M. Rasras, K. Tu, A. E. White, Y. Chen, A. Pomerene, D. Carothers, R. L. Kamocsai, C. M. Hill, and J. Beattie, "CMOS-compatible Si-ring-assisted Mach–Zehnder interferometer with internal bandwidth equalization," *IEEE J. Sel. Topics Quantum Electron*., vol. 16, no. 1, pp. 45–52, Jan./Feb. 2010.

[39] G. Rasigade, D. Marris-Morini, L. Vivien, and E. Cassan, "Perfor- mance evolutions of carrier depletion silicon optical modulators: From p-n to p-i-p-i-n diodes," *IEEE J. Sel. Topics Quantum Electron*., vol. 16, no. 1, pp. 179–184, Jan./Feb. 2010.

[40] G. Rasigade, M. Ziebell, D. Marris-Morini, J.-M. Fédéli, F. Milesi, P. Grosse, D. Bouville, E. Cassan, and L. Vivien, "High extinction ratio 10 Gbit/s silicon optical modulator," *Opt. Exp*., vol. 19, pp. 5827–5832, 2011

[41] A. M. Gutierrez, A. Brimont, G. Rasigade, M. Ziebell, D. Marris-Morini, J.-M. Fédéli, L. Vivien, J. Marti, and P. Sanchis, "Ring-Assisted Mach–Zehnder

Interferometer Silicon Modulator for Enhanced Performance," *J. Lightw. Tech.*, Vol. 30 No. 1, 2012

[42] J. Yang, F. Wang, X. Jiang, H. Qu, M. Wang, and Y. Wang, "Influence of loss on linearity of microring-assisted Mach-Zehnder modulator," *Op. Ex.*, Vol. 12 No. 18 2004

[43] Dingel, B.; Madamopoulos, N.; Prescod, A.; Madabhushi, R., "Analytical model, analysis and parameter optimization of a super linear electro-optic modulator," *Optics Communications*, Volume 284, Issue 24, p. 5578-5587. 2011

[44] E. Ackerman, "Broadband linearization of a Mach–Zehnder electrooptic modulator," *IEEE Trans. Microw. Theory Tech.*, vol. 47, no. 12, pp. 2271–2279, Dec. 1999.

[45] H. Skeie and R. Johnson, "Linearization of electro-optic modulators by a cascade coupling of phase modulating electrodes," *Proc. SPIE–Int. Soc. Opt. Eng.*, vol. 1583, pp. 153–164, Mar. 1991.

[46] S. Korotky and R. DeRidder, "Dual parallel modulation schemes for low-distortion analog optical transmission," *IEEE J. Select. Areas Commun.*, vol. 8, pp. 1377–1381, Sept. 1990.

[47] M. Farwell, Z. Lin, E. Wooten, and W. Chang, "An electrooptic intensity modulator with improved linearity," *IEEE Photon. Technol. Lett.*, vol. 3, pp. 792–795, Sept. 1991.

[48] G. Betts, F. O'Donnell, K. Ray, D. Lewis, D. Bossi, K. Kissa, and G. Drake, "Reflective linearized modulator," in *Proc. Integr. Photon. Res. Conf.*, 1996, pp. 626–629.

[49] K-Y. Tu, M. S. Rasras, D. M. Gill, S. S. Patel, Y-K. Chen, A. E. White, A. Pomerene, D. Carothers, J. Beattie, M. Beals, J. Michel, and L. C. Kimerling, “Silicon RF-Photonic Filter and Down-Converter,” *J. of Lightw. Tech.* , Vol. 28, No. 20, October 15, 2010

[50] R. Sadhwani, B. Jalali, “Adaptive CMOS Predistortion Linearizer for Fiber-Optic Analog Links,” *J. of Lightw. Tech.*, Vol. 21, No. 12, December 2003.

[51] A. Agarwall, T. Banwell, T. K. Woodward, “Optically Filtered Microwave Photonic Links for RF Signal Processing Applications,” *J. Lightw. Tech.*, Vol. 29, No. 16, August 2011.

[52] M. Ziebell, D. Marris-Morini, G. Rasigade, J-M. Fédéli, P. Crozat, E. Cassan, D. Bouville, and L. Vivien, “40 Gbit/s low-loss silicon optical modulator based on a pipin diode,” *Op. Ex*. Vo. 20, Issue 10, pp. 10591-10596, 2012